analytical chemistry

Article

Cite This: *Anal. Chem.* 2019, 91, 12713−12723

pubs.acs.org/ac

Real-Time Measurement of Airborne Carbon Nanotubes in Workplace Atmospheres

Lina Zheng and Pramod Kulkarni*

Centers for Disease Control and Prevention, National Institute for Occupational Safety and Health, Cincinnati, Ohio 45226, United States

Supporting Information

ABSTRACT: With growing applications of carbon nanomaterials, there is a concern over health risks presented by inhalation of carbon nanotube (CNT) aerosol in workplace atmospheres. Current methods used for CNT aerosol measurement lack selectivity to specific form of carbonaceous component or allotrope of interest. Moreover, the detection limits of these methods are also inadequate for short-term monitoring. Here, we describe, for the first time, a near real-time, field-portable instrument for selective quantification of airborne CNT concentration. The approach uses an automated cyclical scheme involving collect-analyze-ablate steps to obtain continuous near real-time measurement using Raman spectroscopy. The method achieves significantly lower detection limits by employing corona-assisted particle microconcentration for efficient coupling with laser Raman spectroscopy. A combination of techniques involving (i) use of characteristic Raman peaks, (ii) distinct ratio of disordered and graphitic peaks, and (iii) principal component classification and regression is employed to identify and quantify the specific form of the aerosolized carbonaceous nanomaterial. We show that the approach is capable of selectively quantifying trace single-walled CNT in the presence of interfering agents such as diesel particulate matter. The detection limit of the method for the single-walled CNT studied in this work was 60 ng m^{-3}, corresponding to a 10 min aerosol collection period, which is significantly lower than that for the NIOSH Method 5040 (~0.15 μg m^{-3} for an 8-h collection on a 25 mm filter at 4 L min^{-1}), a commonly used method for elemental carbon. We demonstrate the automated real-time capability of this field-portable method by continuously measuring a transient single-walled CNT aerosol.

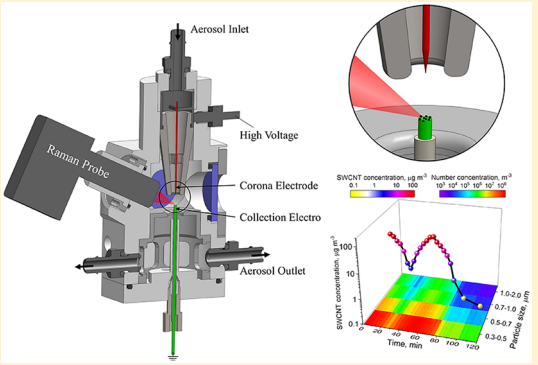

As industrial production of carbon nanotubes (CNTs) and their commercial applications continue to grow,[1] there is an increasing concern about the potential health risks to workers exposed to these materials in aerosolized form in occupational environments. Our understanding of the nature of health risks associated with inhalation exposure to CNTs is still evolving. Animal studies of CNTs have shown that inhalation exposure can lead to fibrosis, cytotoxicity, and mutagenesis.[2−10] A specific type of multiwalled CNT (MWCNT) has been classified as potentially carcinogenic to humans by the International Agency for Research on Cancer (IARC).[11] Insufficient evidence exists for other types of carbon nanotubes. On the basis of the available toxicological evidence and quantitative risk assessment, the National Institute for Occupational Safety and Health (NIOSH) set a recommended exposure limit (REL) for airborne CNTs and carbon nanofibers (CNF) of 1 μg m^{-3}, as an 8-h time weighted average (TWA) for respirable elemental carbon (EC) determined by a modified NIOSH Method 5040.[12] To reduce occupational CNT exposure, accurate and sensitive measurement at low concentrations in air is of critical importance.

Measurement of carbonaceous aerosols in general is of great significance in atmospheric,[12] environmental,[13] and occupational health[3,14] sciences due to the critical role they play in influencing the earth's climate and human health. Measurement of engineered nanomaterials at trace levels, such as CNTs, in industrial workplace atmospheres is often challenging due to the ubiquitous presence of organic and inorganic carbonaceous interfering agents in indoor and outdoor air.[15−17] Moreover, various allotropes of carbon, such as amorphous and graphitic carbon,[18] and fullerenes[19] are often present in anthropogenic combustion aerosols. These factors present challenges in making trace level measurements of specific forms of carbonaceous component of the nanomaterial of interest.

Measurement of carbonaceous aerosols for environmental[20] and occupational health[15,21] applications has involved determination of the EC content of the particulate matter using thermal-optical methods.[21] EC is an operationally defined analyte. In the case of air pollution monitored by thermal-optical reflectance (TOR)[22−24] or thermal-optical transmittance (TOT)[21,25−27] method, it represents the thermally refractory, light-absorbing component of the

Received: May 8, 2019
Accepted: September 10, 2019
Published: September 10, 2019

DOI: 10.1021/acs.analchem.9b02178
Anal. Chem. 2019, 91, 12713−12723

particulate sample collected on a quartz filter.[21] Thermal-optical analysis has been applied to measurement of workplace exposure to diesel particulate matter (DPM), and thermal analysis was later extended to monitor occupational exposure to CNTs.[15,28,29] An EC marker provides selectivity to CNTs,[16] when the EC contribution from other anthropogenic sources is low and the target CNTs contain negligible amorphous carbon impurities.[16,30] The TOT method typically has a detection limit of about 0.15 μg m^{-3} for a full-shift (8-h) air sample collected at 4 L min^{-1} (about 2000 L) on a 25 mm quartz filter.[16] However, typical concentrations of atmospheric EC are in the range of 0.03−2 μg m^{-3},[31,32] which can potentially interfere with the measurement of CNTs using TOR or TOT methods when measuring air concentrations that are close to the REL.

Transmission electron microscopy (TEM) has also been used to obtain selective, but semiquantitative information on air concentration of CNT structures.[33] However, this method is very tedious, and it can take several days to analyze one sample. Moreover, counting statistics and the associated uncertainty in air concentration estimates is often too poor to be meaningful. To address these limitations, Raman confocal microscopy has been used to selectively measure large CNT agglomerates (that are optically visible), which allows faster mapping of larger filter areas to provide better estimates.[30,34] Raman spectroscopy has played a critical role in characterizing fundamental properties of graphitic materials.[35] As a material characterization tool, it can provide fundamental properties of pure graphene and CNTs, such as their crystallite size, presence of sp^2 or sp^3 hybridization, edge structure, strain, number of graphene layers, nanotube diameter (SWCNT), etc.[36] Because of its high specificity, the technique has been applied to the measurement of carbon in various environmental media such as water[37] and air.[38] Braun et al. used Raman confocal microscopy to identify the presence of CNTs in particulate matter collected from the surface of the benchtop of an analytical balance workstation.[34] Lynch et al. recently used a Raman confocal microscope to correlate the occurrence frequency of Raman signal specific to the CNT with EC content of the same sample.[30] However, these approaches, in addition to being cumbersome laboratory methods, suffer from poor detection limits, poor sampling statistics, artifacts related to sample heating and degradation, and/or large measurement uncertainty.

The laboratory methods are resource- and time-intensive; it takes several hours to collect an aerosol sample in the field and hours or days to receive the results back from the laboratory when using either TOT/TOR methods or microscopy. Therefore, these methods are not useful for rapid hazard idenfication on site that is often needed for effective mitigation of hazard exposure. Real-time condensation particle counters and optical particle counters have been used to obtain near-instantaneous concentration of aerosol;[39−42] however, these instruments count all of the sampled particles without any selectivity for the target analyte.

A near real-time approach involving measurement of total atomic carbon at elevated temperature has been used;[17] however, this approach lacks specificity to the carbonaceous component of interest. Currently, no real-time, field-portable methods exist that provide selective measurement of trace airborne CNTs in the presence of interfering carbonaceous components. We present a field-portable instrument based on Raman spectroscopy that minimizes sample degradation and allows near real-time measurement of CNTs at levels well below 1 μg m^{-3}, with robust sampling statistics and superior analytical figures-of-merit.

EXPERIMENTAL SECTION

Instrumentation. Figure 1a shows the overall layout of the instrument system used in this study. The system consists of three key components: an aerosol collection system (i.e., CAM), a compact Raman spectrometer, and a pulsed spark generation system. All key components were controlled through an interface with a data acquisition system and an embedded microcontroller to allow continuous, automated measurements. Airborne particles are sampled through a PM$_1$

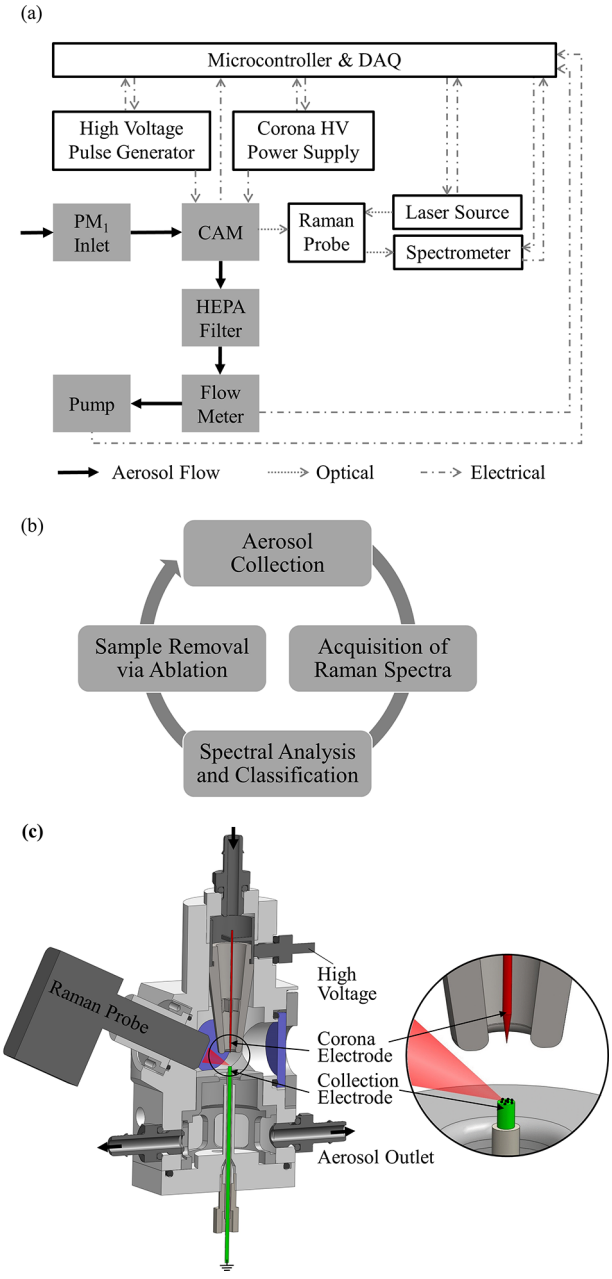

Figure 1. (a) Overall layout of the instrument system used in this study, (b) measurement scheme used for continuous, automated aerosol measurement, and (c) a cross-sectional view of CAM; also shown is the magnified view of the corona and collection electrodes.

DOI: 10.1021/acs.analchem.9b02178
Anal. Chem. 2019, 91, 12713−12723

inlet cyclone into a corona aerosol microconcentrator[43] (CAM), described in detail below, where the particles are collected for analysis on an electrode tip for a predetermined amount of time (typically a few minutes). The particulate sample deposited on the ground electrode is analyzed using a portable Raman system consisting of an integrated Raman probe, a laser source (Innovative Photonic Solutions, Inc., Monmouth Junction, NJ), and a spectrometer (model BWS415-785S-PRB, B&W Tek, Newark, DE). The Raman laser has an excitation wavelength of 785 nm, a maximum power of 572 mW, and a focal spot diameter of 105 μm. The spectrometer has a wavenumber range of 100−3200 cm^{-1} at a spectral resolution of 3.5 cm^{-1}. After the Raman analysis, the particulate sample deposited on the ground electrode is ablated using a sequence of pulsed spark discharges generated by a high voltage pulse generator (Firefly, Cascodium Inc., Andover, MA) with an output energy of 200 mJ per pulse. The sample-free ground electrode is subsequently available for the next cycle of measurement. The aerosol flow through the CAM is driven by a miniature pump and was maintained at 2 L min^{-1} using a proportional-integral-derivative (PID) controller with a feedback from a flowmeter.

Figure 1b shows the overall measurement scheme used in our approach, which consists of the following cyclical steps: (i) collection of particles in the CAM for a predetermined time, (ii) acquisition of Raman spectra at predetermined signal integration time, (iii) spectral analysis and classification to determine CNT type and content, (iv) sample removal via ablation, and (v) return to the first step. These steps were repeated for the desired number of times to obtain semicontinuous automated measurements.

Figure 1c shows the cross-sectional view of the CAM used in our study. The design and collection characteristics of the CAM used by our group have been described in detail elsewhere.[17,43−46] The collection efficiency of the CAM was approximately 65% (Figure S1). The CAM uses two coaxial tungsten electrodes with a separation distance of 3 mm. The corona electrode is 500 μm in diameter and has a sharp tip (with a diameter of 20 μm) for creating a corona, while the collection elecrode is 1 mm in diameter and has a flat tip to provide a planar surface for particle deposition. During aerosol collection in this study, a high positive potential (~4.5 kV) was applied to the corona electrode using a miniature high voltage power supply, and the corona current was maintained at 3 μA using a PID controller. The particles pick up electrical charge from the ions in the corona zone, and subsequently migrate toward the ground electrode where they deposit on its flat tip (Figure 1c). The Raman probe is integrated into the CAM such that the excitation laser is incident at an angle of 45° to the planar collection surface of the ground electrode. The working distance between the probe and the collection surface was 9.5 mm. The Raman scattering was collected by the probe and was analyzed by the spectrometer to obtain the Raman spectra.

Calibration. Calibration curves were obtained for different materials: SWCNT1 (P7-SWNT; Carbon Solutions Inc., Riverside, CA) and DPM (NIST SRM 2975; U.S. Department of Commerce, NIST, Gaithersburg, MD). Test aerosols were generated using a pneumatic atomizer (model 3076, TSI Inc., Shoreview, MN) to aerosolize suspensions prepared by mixing test materials in ultrafiltered DI water (Fisher Scientific, Pittsburgh, PA). The calibration aerosol was passed through a diffusion dryer to remove associated water and then passed through a PM_1 cyclone to obtain particles with aerodynamic diameter less than 1 μm. The particulate mass collected on the ground electrode of CAM was determined from the measured aerosol mass concentration at the inlet of the CAM, volumetric aerosol flow rate, collection time, and the collection efficiency. The mass concentration of the test aerosol was measured using a piezobalance dust monitor (Series 3520; Kanomax USA, Inc., Andover, NJ) and a calibrated DustTrak instrument (model 8533, TSI Inc.). For generating the calibration curve, varying analyte mass levels were obtained by varying the aerosol collection time in CAM from 15 s to 5 min. Calibration curves were constructed by plotting the Raman signal intensity per unit integration time as a function of mass loading on the ground electrode. For each analyte mass level, three replicate Raman measurements were obtained. The average of the three replicate measurements was used to construct the final calibration curve.

Spectral Acquisition and Analysis. The Raman spectra were collected at the maximum power (572 mW) of the excitation laser. Detector integration time ranging from 1 to 3 min was used to optimize the signal-to-noise ratio for a given nanomaterial. Dark and blank spectra subtraction and baseline correction were applied to each spectrum. A baseline drawn tangentially to the spectral curve on each side of the peak was used as a baseline for a given peak Raman frequency shift. In the univariate approach, the signal intensity of a characteristic peak for a given nanomaterial was calculated as the peak height with respect to the peak baseline. In the multivariate approach, partial least squares (PLS) regression was performed on the Raman spectral data for samples with varying analyte mass levels to construct a PLS calibration model, an approach described elsewhere.[46] Principal component analysis (PCA) was performed to identify the type of carbon nanomaterial. PCA and PLS regression were carried out using The Unscrambler 10.0 X (CAMO Analytics Inc., Woodbridge, NJ).

RESULTS AND DISCUSSION

Laser-Induced Sample Heating. Measurement artifacts created by the laser-induced heating in Raman spectroscopy can be of concern for many sample matrixes.[47−49] Sample degradation can occur depending on several factors including laser power density, thermal conductivity of the particuate matrix and the underlying substrate, and the porosity of the particulate sample. For instance, we observed that during Raman measurement of as-received CNT bulk powder sample directly deposited on the tungsten electrode of the CAM, the sample underwent rapid heating and decomposition as seen in the microscope images shown in Figure S2. However, the same CNT sample, when aerosolized and collected as a thin layer on the tungsten electrode of CAM, does not exhibit thermal degradation during Raman analysis (the CNT aerosol has a count median diameter of 54 nm and a geometric standard deviation of 1.7; see Figure S3). This was verified to be the case for different types of CNT and for different aerosolization methods including liquid atomization and dry dispersion. In this case, the heat conduction to the conductive tungsten substrate is more efficient, and the substrate acts as an effective heat sink for the particles.[50,51]

A series of Raman spectra for aerosolized SWCNT1 collected on the tungsten ground electrode of the CAM were obtained for various nominal laser power density levels ranging from 1.2 to 6.6 kW cm^{-2} (Figure S4). The peak intensity (I_P) at the characteristic Raman frequency shift at 166

DOI: 10.1021/acs.analchem.9b02178
Anal. Chem. 2019, 91, 12713−12723

cm^{-1} (radial breathing mode; RBM) increases linearly with the power density of the laser (Figure 2a, red square). Studies have

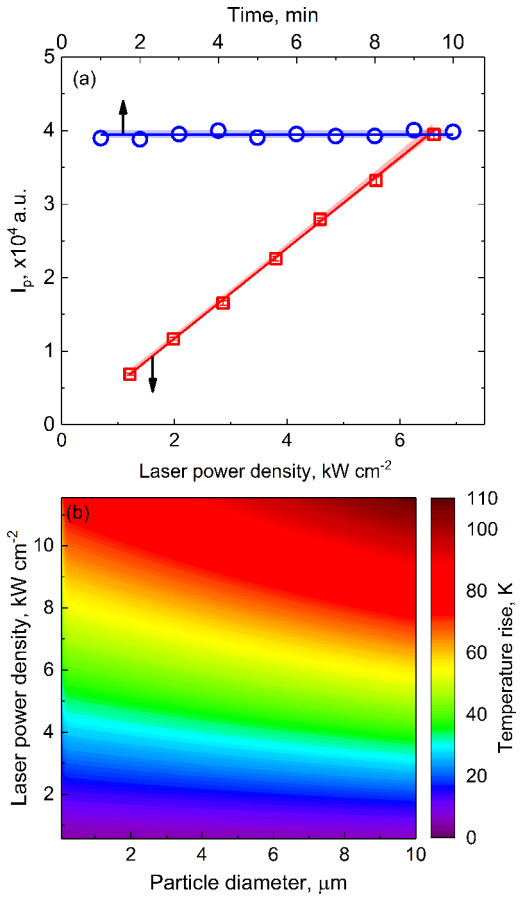

Figure 2. (a) Variation of the RBM peak signal intensity as a function of nominal laser power (red square symbol); also shown are consecutive measurements (each at detector integration time of 60 s) over 10 min continuous irradiation of the same sample spot (shown by blue circles) at the highest laser power density (6.6 kW cm^{-2}); the excitation laser was turned on at all times during the 10 min duration; the shaded areas represent 95% confidence bands. (b) Sample temperature rise as a function of particle diameter and laser power computed using one-dimensional heat transfer model.

shown that sample heating can induce a small change in Raman frequency shift in some materials.[52,53] Measurements at elevated power densities in our study showed frequency shifts less than 0.2% of the mean value, implying minimal heating. In addition, as shown in Figure 2a, we obtained a series of consecutive Raman measurements of the same deposited SWCNT1 over 10 min (at the highest laser power density of 6.6 kW cm^{-2}) to simulate prolonged sample irradiation times. The signal intensity was practically the same for each of the periodic measurements over the 10 min duration (relative standard deviation of 1% around mean value). These observations suggest that the laser-induced heating for airborne CNT deposited on the CAM electrode is negligible for nominal laser power of up to 6.6 kW cm^{-2}. Theoretical estimates of temperature rise from laser-induced heating qualitatively support our experimental observations noted above. These calculations were performed using a one-dimensional heat transfer model following an approach described by Rosasco et al.[51] The details of the calculation are presented in section S2 of the Supporting Information. The model assumes a layer of particulate sample with known thermal conductivity and layer thickness deposited on a known substrate. The results of these calculations are summarized in Figure 2b, which shows variation of temperature rise of the particulate matrix as a function of particle diameter and the nominal laser power. The temperature rise increases with increasing particle diameter and laser power. For a particle with diameter of 1 μm, the temperature rise was estimated to be 46 K at the highest laser power density studied (6.6 kW cm^{-2}); for a 4 μm particle the rise was 53 K, suggesting only mild heating for the respirable[54] aerosol size range. Such mild temperature rise is unlikely to cause thermal degradation of carbonaceous particles studied in this work.[55−57] On the other hand, for particles as large as 500 μm diameter, the temperature rise could be as high as 1000 K. Heat transfer from a larger CNT particle (which is a poor thermal conductor) to the heat sink (i.e., the tungsten electrode) is less efficient as compared to that for smaller particles. These calculations are consistent with our experimental observations of as-received bulk CNT samples, which readily decompose when irradiated with the Raman excitation laser (see Figure S2). However, our experimental results and calculations suggest negligible artifacts from laser-induced heating for respirable aerosol collected in CAM.

Calibration. Figure 3a shows Raman spectra of SWCNT1 aerosol at different particulate mass collected in CAM. The SWCNT1 exhibits four characteristic bands: the radial breathing mode (RBM; 166 cm^{-1}), the disorder peak (D mode, 1314 cm^{-1}), the tangential vibrational mode (G mode; 1594 cm^{-1}), and the second order overtone of the D mode (2D; 2592 cm^{-1}). The RBM mode is a unique characteristic band for SWCNTs, which corresponds to the symmetric in-phase displacements of all of the carbon atoms in the radial direction. The D-band corresponds to defective graphitic structures near the edge of the microcrystalline structure. The G-band corresponds to the in-plane stretching vibrations of graphitic sp^2 carbon atoms.[35]

From Figure 3a, the peak intensity at characteristic frequency shift (referred to here as peak Raman signal intensity [I_P] or peak height) increases with increasing analyte mass. Figure 3b shows the corresponding calibration curves for SWCNT1 using different vibrational modes. Raman signal intensity was normalized by the detector integration time to construct these calibration curves. All calibration curves could be described using a linear regression fit with an $R^2 > 0.98$. For a given material type, the measurement sensitivity varied depending on which vibrational mode was used. The RBM mode provided the most sensitive measurement for SWCNT1. The measurement sensitivity of different types of SWCNT may vary depending on the properties of the SWCNT such as the nanotube diameter, chirality, and chemical composition. Calibration for each target SWCNT type may be necessary for reliable measurement. Each point on the calibraiton curve represents an average over three replicates. The error bar represents the standard deviation around the mean; the relative standard deviation was in the range 2−15% (with a mean value of 6.7%). This level of precision or repeatability is deemed acceptable for exposure monitoring applications.[58]

DPM was used in this study to mimic the background carbonaceous interfering agent, because it is present in many workplace aerosols[14,59−61] and may potentially interfere with selective CNT measurement. Raman spectra of the certified

DOI: 10.1021/acs.analchem.9b02178
Anal. Chem. 2019, 91, 12713−12723

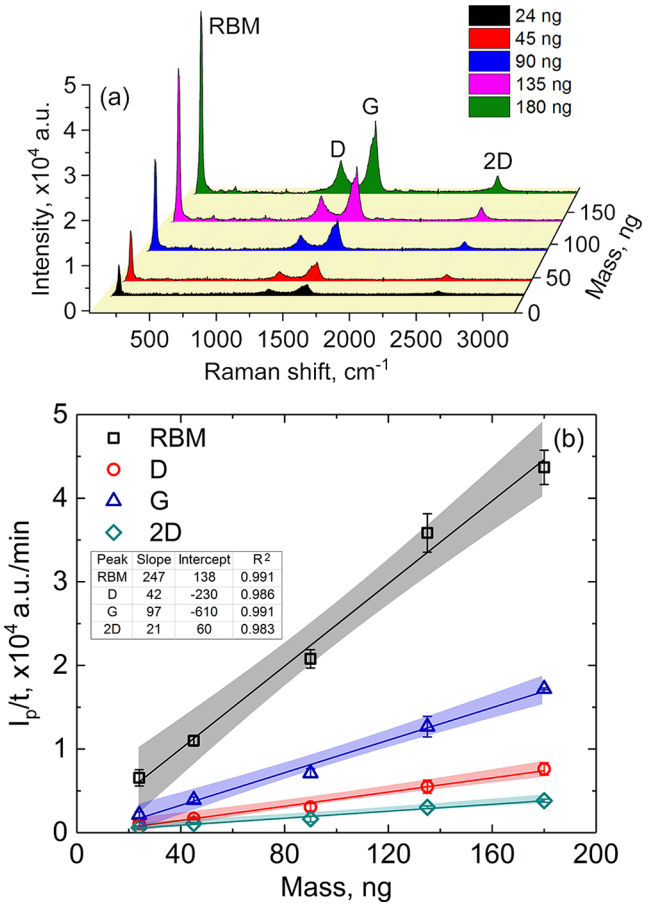

Figure 3. (a) Raman spectra of SWCNT1 deposited on the collection electrode at different mass loadings, and (b) calibration curves for SWCNT1 constructed by plotting peak signal intensity per unit integration time as a function of mass loading on the ground electrode of CAM. Measurement integration time was 1 min. The lines represent linear fits to the experimental data. The error bars represent standard deviations of three replicate measurements. The shaded areas represent 95% confidence bands.

DPM standard and the corresponding calibration curves are shown in Figure S5. The certified DPM standard used in this study exhibits two overlapping peaks at 1320 and 1594 cm^{-1} (i.e., D and G bands), consistent with earlier studies.[62−64]

Detection Limits. The LOD was estimated using 3-sigma criteria defined by the International Union of Pure and Applied Chemistry (IUPAC).[65] Details on the determination of LOD are provided in section S4 of the Supporting Information. Table 1 shows the LODs for SWCNT1 and DPM in terms of mass and air concentration obtained from the calibration curves in Figures 3b and S6b. At a signal integration time of 3 min, the mass LOD was 0.9 ng for SWCNT and 8.1 ng for DPM. The LODs in terms of air concentration were obtained for different aerosol collection times of 2, 10, and 20 min by using a Raman signal integration time of 3 min and a sampling flow rate of 2 L min^{-1}. Using a collection time of 20 min, the LOD in terms of air concentration was estimated to be 0.03 μg m^{-3} for SWCNT1 and 0.3 μg m^{-3} for DPM. Lower LODs could be achieved by further increasing the aerosol collection time in CAM.

The LOD corresponding to a 20 min collection period and analysis by our Raman method is significantly lower than that of the TOT/TOR methods. The LODs of thermal-optical

Table 1. Limits of Detection for Determination of SWCNT1 and DPM Using Our Raman Method

	LOD in terms of mass, ng	
integration time, min	SWCNT1	DPM
1	1.6	12
2	1.2	10
3	0.9	8.1
	LOD in terms of concentration,[a] μg m^{-3}	
sample collection time, min	SWCNT1	DPM
2	0.35	3.1
10	0.06	0.6
20	0.03	0.3

[a]Assuming a Raman integration time of 3 min, a sampling flow rate of 2 L min^{-1}, and a collection efficiency of 65%.

methods for EC corresponding to the 8-h aerosol collection range from 0.07 to 3.4 μg m^{-3}.[21,66,67] The drastic improvement in sensitivity of our system is accomplished by collection of particles over a small spot in CAM, which allows effective coupling with the Raman excitation laser.

We anticipate that these limits of detection will hold in the presence of large amounts of DPM or atmospheric black carbon in the particulate matrix, in excess of ratios studied in this work. On the basis of the 1-D heat-transfer model discussed earlier, we estimate the temperature rise induced by the Raman laser in a 10-μg particulate sample to be only about 55 K. This rise is much lower than the ignition temperature for SWCNT of 620 K.[68] Assuming a ratio of SWCNT to EC of 1:1000, the amount of SWCNT associated with 10 μg of EC is 10 ng, which is much larger than the mass detection limits in Table 1. These calculations suggest that measurements could be made at these detection limits without introducing sample heating artifacts in the presence of large amounts of DPM or black carbon.

Selective CNT Measurement. To further probe the selectivity of our method, we used a mixed aerosol generated by mixing the aerosolized SWCNT1 with the interfering agent DPM in different proportions (see section S5 on the measurement of nanomaterials in the presence of DPM in the Supporting Information for details). The DPM in the mixed aerosol was meant to simulate the broad range of interfering levels of EC, for instance, from the outdoor or indoor ambient air or from automobile emissions. Figure 4 shows Raman spectra for SWCNT1 aerosol (pink), DPM aerosol (gray), and mixed aerosol containing both SWCNT and DPM samples (blue). The total mass loading of each sample, and the relative composition of DPM and SWCNT1 for each sample, are shown using the pie charts adjacent to each sample spectrum in Figure 4. Four mixed aerosol samples were tested, with varying ratios of SWCNT1 to DPM, ranging from 1:20 to 1:2. These ratios are comparable to those typically expected in the workplace atmospheres (see section S6 in the Supporting Information). Raman spectra of mixed aerosol for all of the samples show the RBM mode. As expected, Raman spectra of pure SWCNT1 aerosol and the mixed aerosol suggest that the Raman signal intensity of the RBM peak only depended on the SWCNT1 mass, regardless of the DPM content, ruling out any potential interference.

Figure 5 shows the comparison of TOT and Raman measurements for a mixed aerosol containing SWCNT1 and DPM. EC concentrations were measured using the TOT

DOI: 10.1021/acs.analchem.9b02178
Anal. Chem. 2019, 91, 12713−12723

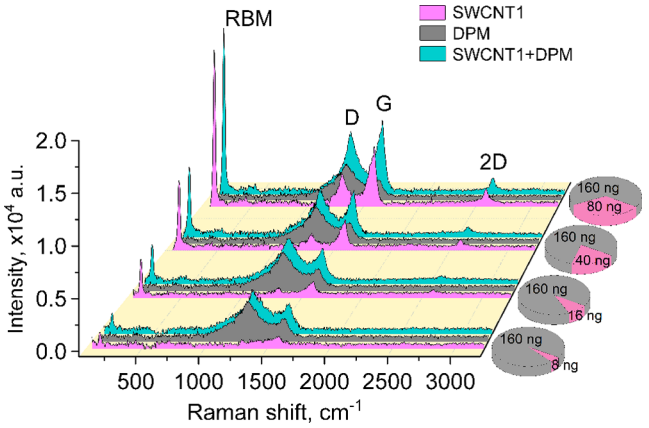

Figure 4. Raman spectra of various test aerosols: (i) SWCNT1, (ii) DPM, and (iii) mixture of SWCNT1 and DPM aerosol. The proportion of SWCNT1 and DPM in each of the mixed aerosol sample is shown in the pie charts.

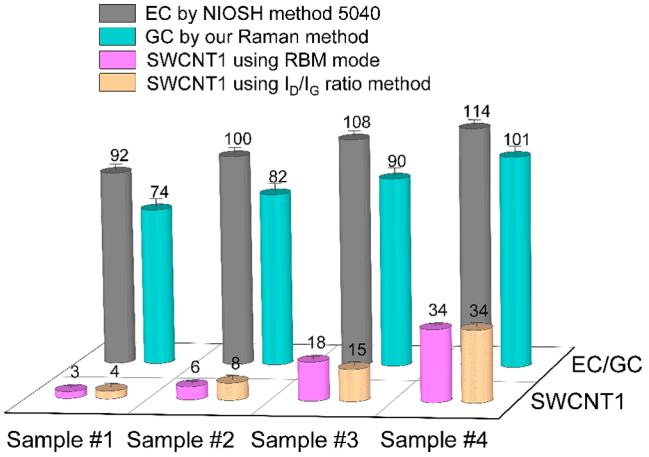

Figure 5. Comparison of graphitic carbon (GC) and specific SWCNT1 air concentrations measured using our Raman method with the elemental carbon (EC) concentrations obtained by thermal-optical analysis (NIOSH Method 5040 with manual split). The test aerosol was a mixture of SWCNT1 and DPM aerosol in varying proportions. The SWCNT1-to-DPM ratios of the four test aerosol samples are 1:2, 1:4, 1:10, and 1:20, respectively.

method (NIOSH Method 5040). Here, we define a term "graphitic carbon" (GC) to quantify the carbonaceous components represented by both the D and the G vibrational modes in the Raman spectrum. Earlier studies have defined similar graphitic carbon content using the G mode only.[69,70] However, here we also include the D mode to account for the disordered graphitic mode. A linear calibration curve was constructed for the determination of GC by relating the area below the D and G peaks of the Raman spectrum with the corresponding mass of SWCNT1. We also note these two modes overlap with the D_3 mode corresponding to the amorphous carbon. Therefore, our GC estimate also includes contribution from amorphous carbon (D_3 mode). In principle, the contribution of D_3 mode should be subtracted; however, its contribution was negligible for most samples in this study. The air concentration of GC ($\mu g\ m^{-3}$) was obtained using the aerosol flow rate, the collection efficiency, and the collection time. The SWCNT1 concentration was determined using the calibration curve constructed using the RBM mode. In addition, GC and SWCNT1 concentrations were also measured using the G and D peaks. Although both EC and GC are not equivalent measurements, both represent the graphitic and amorphous carbon content of the sample (the GC also includes contribution from D_3 as noted above). It is likely that these two estimates are close to each other for most carbonaceous materials with sp^2 hybridization (except in cases where there could be significant interference in TOR or TOT measurement from charring).

Because both SWCNT1 and DPM contribute to G and D modes, an approach was developed to subtract the contribution from SWCNT1 to these modes to obtain the contribution from only the non-SWCNT1 carbonaceous component. The G mode is from in-plane stretching vibration of carbon atoms pairs. This mode is always active, and it is characteristic of all materials with sp^2 structures, including CNT, graphene, and graphite. The D mode is from an in-plane breathing vibration of the aromatic ring involving motion of the six atoms. This band is active only in the presence of disorders and in nonideal structures. The ratio of D and G band intensities provides an estimate of the amount of defects in the graphitic structure; this ratio is inversely proportional to the size of the ordered sp^2 domain (L), given by the relationship: $L = [2.4 \times 10^{-10} \cdot \lambda_e^4 \cdot (I_D/I_G)^{-1}]$, where I_D and I_G are the integrated intensities of the D and G peaks, and λ_e is the excitation wavelength in the range of 458−645 nm.[71−73] Assuming this equation is applicable to 785 nm excitation laser, the ordered sp^2 domain size was estimated to be 182 nm for SWCNT1 and 16 nm for DPM in our study.

Comparisons in Figure 5 show that the GC estimates from our Raman method are within 16% (normalized root mean squared error [RMSE]) of the EC estimates from the TOT method, while SWCNT1 estimates are significantly lower than the EC value from the TOT method. For the four test aerosol samples, the ratios of measured air concentration of SWCNT1 to GC using our method were 4%, 7%, 20%, and 32%, respectively. These ratios agreed well with the corresponding predetermined ratios (by mass) (5%, 9%, 20%, and 33%) in the mixed test aerosol containing SWCNT1 and DPM. The error bars show the standard deviation around the mean of three replicate measurements. The relative standard deviations were in the range of 4−11% for our Raman method, and 0−9% for the TOT method.

Results in Figure 5 clearly demonstrate that using the RBM peak, the Raman method can provide selective measurement of SWCNT even when other carbonaceous components are present. Alternatively, one can also retrieve the CNT concentration using the peak intensities at G and D modes and their distinct ratio (I_G/I_D) (see section S7 on SWCNT quantification using D and G modes in the Supporting Information for details). We compared this alternate I_G/I_D ratio approach with the RBM mode method; the results were comparable as shown in Figure 5. The normailized RMSE was 12%.

For measurement of SWCNTs, the RBM mode provides high specificity. However, for other nanomaterials such as MWCNT and graphene that do not exhibit the RBM mode, the I_G/I_D ratio approach can be used to obtain reliable estimates of graphitic carbon component associated with only the nanomaterials. Such an approach has been used to distinguish functionalized MWCNTs,[74] emissions from aircraft engines,[75] and DPM.[76]

Identification of Type of Carbon Nanomaterials. The G mode, which is common to all graphitic materials, has

DOI: 10.1021/acs.analchem.9b02178
Anal. Chem. 2019, 91, 12713−12723

distinct shape for each material and can be used to distinguish the nanostructures.[36] These distinct shapes of G and D modes can be further revealed by deconvoluting the measured spectrum into underlying separate modes that correspond to different phonon transitions within graphene layers.[77,78] Figure S7 shows the measured D and G peaks, along with the deconvoluted bands,[77] for various carbon nanomaterials studied in this work. The Raman spectrum of DPM is deconvoluted into five bands including four Lorentzian bands (G, D, D_2, D_4) and a Gaussian band (D_3).[77] The Raman spectra of SWCNT1, MWCNT1, and graphene are deconvoluted into three bands (G, D, D_3). The D_2 band is related to the presence of incomplete graphitic structure at the borders of crystallites, which stretches C−C bonds; the D_3 band is associated with amorphous carbon; and the D_4 band is related to the presence of impurities in the DPM such as ions, metals, and polyenes.[79] Table S2 shows a comparison of full width at half-maximum (fwhm) of the D and G modes, and the I_G/I_D ratio obtained for the four carbon nanomaterials. The fwhm of the D mode and the ratio I_G/I_D are distinct for all four carbon nanomaterials.

To further identify the type of carbon nanomaterial, classification using the PCA of Raman spectra was conducted for all of the nanomaterials studied in this work. Figure 6

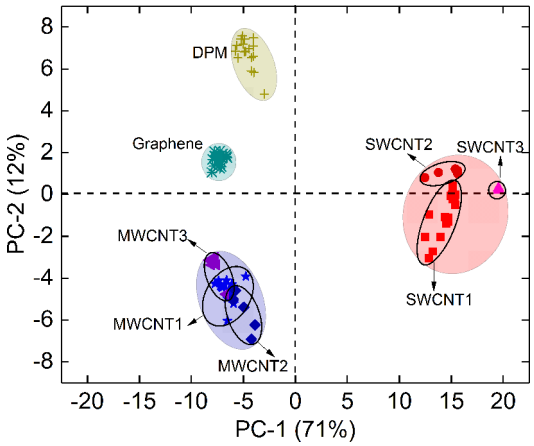

Figure 6. PCA classification analysis of Raman spectra for various carbon nanomaterials showing scores plot using two principal components.

shows the result of this classification analysis. Raman spectra from three single-walled nanotube materials (labeled as SWCNT1, SWCNT2, and SWCNT3), three multiwalled carbon nanotube materials (labeled as MWCNT1, MWCNT2, and MWCNT3), graphene, and DPM were used for classification. The nomenclature used for these materials is provided in Table S3. Representative Raman spectra of these materials are shown in Figure S8. The PCA model was constructed using the Raman shift frequency in the range 800−1800 cm^{-1}, which includes the D and G modes. The spectra were preprocessed by applying the blank and baseline correction and standard normal variate (SNV) normalization.[80] The first and second principal components (PC1 and PC2) accounted for 83% of the total variance in the data (71% and 12%), and were used to generate the scores plot. The loadings plot for PC1 and PC2 are included in section S8 of the Supporting Information. As seen in Figure 6, the classification yields distinct clusters, each representing a different material. Small variations were observed within each cluster, for instance, various multi- and single-walled CNTs clustered in three subgroups as seen in Figure 6. This demonstrates the ability of this approach to identify the type of carbon nanomaterial. This algorithm can be readily implemented for automated classification and identification of unknown carbonaceous aerosol type in the workplace air.

MWCNT Quantification Using D and G Modes. We used PLS[46] regression of spectral data containg D and G modes to develop a calibration model and subsequently apply it to quantify the CNT content in the presence of DPM interfering agent. This method is required for MWCNT and graphene particles, which do not exhibit the RBM mode in their Raman spectrum. A calibration model using PLS regression was constructed by preparing training samples containing a mixture of MWCNT1 and DPM in various proportions. The total mass of MWCNT1 and DPM in these training set suspensions was kept the same, while the ratio of MWCNT1 to DPM mass (in the suspension) was varied. The fraction of MWCNT1 in these samples was systematically varied to cover a range of 0.1−1. Raman spectra for particulate samples containing different MWCNT1 fractions were then obtained. PLS regression of these Raman spectra was then performed to correlate with the fractional content of MWCNT1. Random cross validation was used involving five segments with four samples per segment. The cross validation results of PLS regression showed a strong correlation between the predicted and known MWCNT1 fractions (i.e., the percentage of MWCNT in the mixed sample), with an R^2 = 0.92 (Figure 7). The model was tested on an aerosol with

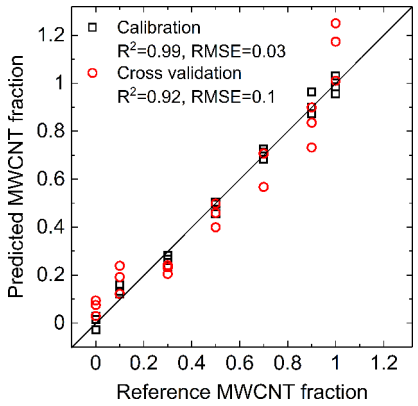

Figure 7. Predicted versus reference MWCNT1 fractional content obtained using the PLS regression model.

unknown MWCNT1 fraction, and was able to predict the fractional content within the RMSE of 0.1. It should be noted that for this approach to be applicable, a priori knowledge of the number and types of carbonaceous components and their Raman spectra is essential. We expect this approach to provide reliable quantification in a two-component system, for instance, where a single type of carbon nanomaterial is to be measured in the presence of black carbon or DPM. The reliability may also depend on how well the training sample set is designed for PLS calibration. The applicability of this approach for aerosols containing more than two distinct carbonaceous materials is unknown; it may not be effective for aerosols containing multiple types of nanomaterials.

Variability of Raman spectra of DPM (across different sources) or atmospheric black carbon can also affect the

DOI: 10.1021/acs.analchem.9b02178
Anal. Chem. 2019, 91, 12713−12723

usefulness of this approach. To probe this variability, we measured Raman spectra of various background aerosols containing black carbon that may potentially interfere with selective CNT measurement. These aerosols included direct exhaust emissions from various diesel engines as well as indoor workplace aerosols containing DPM or outdoor atmospheric black carbon. Our measurements show that the Raman spectra of all of these carbonaceous aerosols, containing DPM or atmospheric black carbon, have similar spectral characteristics, due to their similar graphitic carbon content. The peak height ratios and peak widths of D and G peaks for various aerosols are presented in Table S4. The table also shows deviation of these metrics from those for the NIST SRM, which are in the range of 1−13%. The similarity of DPM and black carbon from various occupational and environmental sources eliminates the need to measure the background (or interferant) aerosol for each application, and considerably improves the efficacy of PCA classification and PLS regression approach across various workplaces.

It has been shown that Raman spectra of single- and double-walled carbon nanotubes can shift due to oxidation at high temperatures >300 °C;[81,82] however, it is not known if such shift is possible under conditions typical in indoor workplace environments. It is important to ensure that the spectral features of CNT in the unknown samples are consistent with those of the calibration aerosol to allow reliable quantification.

Real-Time Measurement Capability. Figure 8 demonstrates the near real-time capability of our Raman method for measurement of transient SWCNT1 aerosol. A test aerosol containing SWCNT1 was generated in the laboratory; the aerosol concentration was varied in the test chamber to simulate a transient aerosol over a period of 2 h. The air concentration of the SWCNT1 was varied from 0.15 to 55 μg m^{-3}. The particle size distribution of the test aerosol was continuously measured using an optical particle counter and is shown as a color contour map in the $x-y$ plane in Figure 8. Simultaneously, the SWCNT1 mass concentration of the same test aerosol was also continuously measured using our automated Raman method, and is shown in Figure 8 by the line plot. The markers on the line plot are color-coded to show the SWCNT1 air concentration at corresponding times. Higher SWCNT1 concentrations were measured at a time resolution of 4 min (including 2 min for sample collection, 1 min for Raman analysis, and 1 min for sample ablation). Lower SWCNT1 concentrations below 1 μg m^{-3} required longer sampling times of 18 min. As the total number concentration of the SWCNT1 aerosol decreased from 1.85 × 10^8 to 1.44 × 10^6 m^{-3}, the SWCNT1 mass concentration decreased from 55 to 0.15 μg m^{-3}.

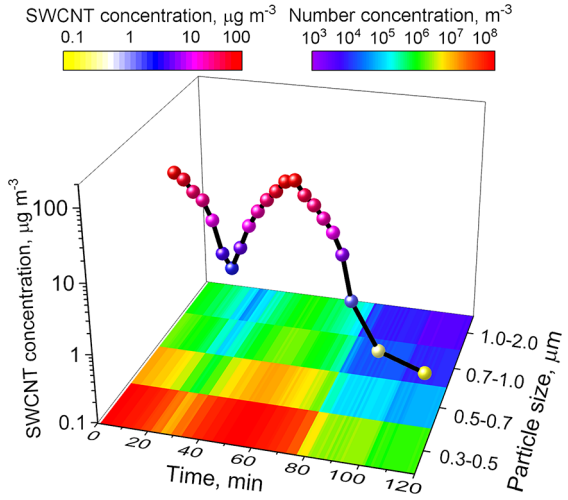

Figure 8. Real-time measurement of airborne SWCNT mass concentration (scatter and line plot) using Raman spectroscopy. The markers are color-coded to show SWCNT concentration. Size- and time-resolved particle number concentration of the same aerosol, measured separately (and simultaneously) by an optical particle counter, is shown as a contour plot in the $x-y$ plane.

These measurements clearly demonstrate the capability of our approach to obtain continuous, automated near real-time measurements. We note that while few studies have reported real-time measurement of chemical speciation of aerosols using Raman spectroscopy,[83−85] this is the first study, to our knowledge, that presents a method that optimizes sensitivity, sampling statistics, accuracy, and precision for a meaningful measurement of aerosols, specifically airborne nanomaterials. Many of the previous studies[83−85] involved Raman analysis of aerosol particles in suspended state. Because Raman scattering is orders of magnitude weaker than the elastic scattering, these approaches suffered from very poor sampling statistics and detection limits (typically >1 mg m^{-3}),[83−85] due to an exceedingly small amount of sample probed. Moreover, free-stream analysis of suspended particles (in air/gas) requires larger lasers with orders of magnitude higher power density and carefully designed optics to obtain a small focused spot to induce Raman scattering, making this approach unsuitable for field-portable instrumentation. Some recent studies have reported field-portable instruments that involve Raman analysis of collected particles on a substrate that have improved detection limits.[86−88] Our method provides superior time resolution and detection limits, and it is field-portable. While this study did not focus on fabrication of an actual field-portable prototype, all of the key components, including the CAM cell, electrical and mechanical components, pump, and the spetroscopy system, were designed for inclusion in a compact, battery-operated, hand-portable instrument. A field-portable prototype is currently under construction.

Depending on the nature of the sample, heating and fluorescence can affect the applicability of our method, as is the case with any conventional Raman measurement. We note that one of the key advantages of our approach is negligible or reduced sample heating due to efficient heat transfer to the metal electrode of CAM. Our calculations suggest that sample heating may not be a concern for most carbonaceous materials. Raman studies of carbon nanomaterials typically employ shorter excitation wavelengths such as 514, 532, or 633 nm;[79,89−92] however, 785 nm wavelength used in this study was found to provide adequate sensitivity with minimal fluorescence.

CONCLUSIONS

We have described a field-portable instrument for near real-time, sensitive measurement of airborne CNT concentrations in workplace atmospheres using a portable Raman spectrometer. We demonstrate that the method addresses several key challenges pertaining to trace measurement of aerosols using Raman spectroscopy: (i) it eliminates sample heating and decomposition typical for highly light-absorbing carbon nanomaterials, (ii) it incorporates efficient aerosol collection and interface for semicontinuous and automated Raman

DOI: 10.1021/acs.analchem.9b02178
Anal. Chem. 2019, 91, 12713−12723

analysis, (iii) it drastically improves sensitivity, sampling statistics, and time resolution compared to current filter methods, and (iv) it allows near real-time measurement in a hand-portable instrument. The detection limit of our method for SWCNT studied in this work was determined to be 60 ng m^{-3} at a time resolution of 10 min, which is approximately 2−3 orders of magnitude lower than that of the standard thermal-optical method using the same sampling time. We employed a combination of different techniques to selectively identify a nanomaterial and quantify its air concentration; these techniques included: (i) use of unique characteristic Raman vibrational modes for each nanomaterial, (ii) characteristic ratio of D and G modes for each nanomaterial, and (iii) principal component classification and regression. We show that the method is capable of selectively quantifying trace SWCNT in the presence of large interference from DPM. The RBM mode in SWCNTs offers excellent selectivity to SWCNT. For other nanomaterials (that do not exhibit the RBM mode), calibration using PLS regression of the spectral data (in D and G mode) obtained from a training sample set could possibly provide selective quantification of one type of nanomaterial in the presence of interfering DPM. The superior detection limits, sampling statistics, and time resolution of our Raman method make it well-suited for the development of a hand-held instrument for monitoring of aerosol in workplace atmospheres.

■ ASSOCIATED CONTENT

Supporting Information

The Supporting Information is available free of charge on the ACS Publications website at DOI: 10.1021/acs.analchem.9b02178.

Collection efficiency of CAM; calculation of laser-induced sample temperature rise; calibration for DPM; determination of LOD; measurement of nanomaterials in the presence of DPM; ratio of SWCNT to atmospheric black carbon (BC) or elemental carbon (EC); SWCNT quantification using D and G modes; loadings plot for PC1 and PC2; Tables S1−4; and Figures S1−9 (PDF)

■ AUTHOR INFORMATION

Corresponding Author

*Phone: (513) 841-4300. Fax: (513) 841-4545. E-mail: pskulkarni@cdc.gov.

ORCID

Lina Zheng: 0000-0002-6830-8058

Pramod Kulkarni: 0000-0001-7692-4662

Notes

The findings and conclusions in this paper are those of the authors and do not necessarily represent the views of NIOSH. Mention of company names and products does not constitute endorsement by NIOSH.

The authors declare no competing financial interest.

■ ACKNOWLEDGMENTS

This research was supported by the NIOSH intramural grants from the National Occupational Research Agenda and NIOSH Nanotechnology Research Center. We would like to thank Drs. Eileen Birch and Matthew Dahm for providing thoughtful comments and feedback on this work.

■ REFERENCES

(1) Schiavo, A. *Carbon Nanomaterials Update 2016*; Lux Research: Boston, MA, 2016.

(2) Lam, C.-W.; James, J. T.; McCluskey, R.; Hunter, R. L. *Toxicol. Sci.* **2003**, *77* (1), 126−134.

(3) Lam, C.-w.; James, J. T.; McCluskey, R.; Arepalli, S.; Hunter, R. L. *Crit. Rev. Toxicol.* **2006**, *36* (3), 189−217.

(4) Shvedova, A. A.; Kisin, E.; Murray, A. R.; Johnson, V. J.; Gorelik, O.; Arepalli, S.; Hubbs, A. F.; Mercer, R. R.; Keohavong, P.; Sussman, N. *Am. J. Physiol. Lung Cell Mol. Physiol.* **2008**, *295* (4), L552−L565.

(5) Ma-Hock, L.; Treumann, S.; Strauss, V.; Brill, S.; Luizi, F.; Mertler, M.; Wiench, K.; Gamer, A. O.; Van Ravenzwaay, B.; Landsiedel, R. *Toxicol. Sci.* **2009**, *112* (2), 468−481.

(6) Aschberger, K.; Johnston, H. J.; Stone, V.; Aitken, R. J.; Hankin, S. M.; Peters, S. A.; Tran, C. L.; Christensen, F. M. *Crit. Rev. Toxicol.* **2010**, *40* (9), 759−790.

(7) Porter, D. W.; Hubbs, A. F.; Chen, B. T.; McKinney, W.; Mercer, R. R.; Wolfarth, M. G.; Battelli, L.; Wu, N.; Sriram, K.; Leonard, S. *Nanotoxicology* **2012**, *7*, 1179−1194.

(8) van Berlo, D.; Wilhelmi, V.; Boots, A. W.; Hullmann, M.; Kuhlbusch, T. A.; Bast, A.; Schins, R. P.; Albrecht, C. *Arch. Toxicol.* **2014**, *88* (9), 1725−1737.

(9) Sargent, L. M.; Porter, D. W.; Staska, L. M.; Hubbs, A. F.; Lowry, D. T.; Battelli, L.; Siegrist, K. J.; Kashon, M. L.; Mercer, R. R.; Bauer, A. K. *Part. Fibre Toxicol.* **2014**, *11* (1), 3.

(10) Rydman, E. M.; Ilves, M.; Vanhala, E.; Vippola, M.; Lehto, M.; Kinaret, P. A.; Pylkkänen, L.; Happo, M.; Hirvonen, M.-R.; Greco, D. *Toxicol. Sci.* **2015**, *147* (1), 140−155.

(11) Yann, G.; Dana, L.; Guyton, K. Z.; Secretan, B. L.; El Ghissassi, F.; Véronique, B.; Tallaa, L. B.; Neela, G.; Chiara, S.; Heidi, M. *Lancet Oncol.* **2014**, *15*, 1427−1428.

(12) Bond, T. C.; Doherty, S. J.; Fahey, D.; Forster, P.; Berntsen, T.; DeAngelo, B.; Flanner, M.; Ghan, S.; Kärcher, B.; Koch, D. *J. Geophys. Res. Atmos.* **2013**, *118*, 5380−5552.

(13) Yttri, K. E.; Myhre, C. L.; Torseth, K. *World Meteorological Org. (WMO) Bull.* **2009**, *58*, 54.

(14) Cantrell, B. K.; Watts, W. F., Jr *Appl. Occup. Environ. Hyg.* **1997**, *12* (12), 1019−1027.

(15) Birch, M. E.; Ku, B.-K.; Evans, D. E.; Ruda-Eberenz, T. A. *Ann. Occup. Hyg.* **2011**, *55*, 1016−1036.

(16) NIOSH, Current Intelligence Bulletin 65: Occupational Exposure to Carbon Nanotubes and Nanofibers. DHHS (NIOSH) Publication No. 2013-145: Cincinnati, OH, 2013.

(17) Zheng, L.; Kulkarni, P.; Birch, M. E.; Deye, G.; Dionysiou, D. D. *Aerosol Sci. Technol.* **2016**, *50* (11), 1155−1166.

(18) Maricq, M. M. *J. Aerosol Sci.* **2007**, *38* (11), 1079−1118.

(19) Encinas, D.; Gómez-de-Balugera, Z. *Arch. Environ. Contam. Toxicol.* **2018**, *75* (4), 616−624.

(20) Schauer, J. J. *J. Exposure Sci. Environ. Epidemiol.* **2003**, *13* (6), 443.

(21) Birch, M. E.; Cary, R. A. *Aerosol Sci. Technol.* **1996**, *25* (3), 221−241.

(22) Chow, J. C.; Watson, J. G.; Chen, L.-W. A.; Chang, M. O.; Robinson, N. F.; Trimble, D.; Kohl, S. *J. Air Waste Manage. Assoc.* **2007**, *57* (9), 1014−1023.

(23) Han, Y.; Cao, J.; Chow, J. C.; Watson, J. G.; An, Z.; Jin, Z.; Fung, K.; Liu, S. *Chemosphere* **2007**, *69* (4), 569−574.

(24) Pavlovic, J.; Kinsey, J.; Hays, M. *Atmos. Meas. Tech.* **2014**, *7* (9), 2829−2838.

(25) Bauer, J. J.; Yu, X.-Y.; Cary, R.; Laulainen, N.; Berkowitz, C. *J. Air Waste Manage. Assoc.* **2009**, *59* (7), 826−833.

(26) Chow, J.; Watson, J.; Chen, L.-W.; Paredes-Miranda, G.; Chang, M.-C.; Trimble, D.; Fung, K.; Zhang, H.; Zhen Yu, J. *Atmos. Chem. Phys.* **2005**, *5* (11), 2961−2972.

(27) Peterson, M. R.; Richards, M. H. *Thermal-Optical-Transmittance Analysis for Organic, Elemental, Carbonate, Total Carbon, and OCX2 in PM2.5 by the EPA/NIOSH Method*; Proceedings, Symposium on Air Quality Measurement Methods and Technology-2002; Air & Waste Management Association: Pittsburgh, PA, 2002; p 83-1.

DOI: 10.1021/acs.analchem.9b02178
Anal. Chem. 2019, 91, 12713−12723

(28) Dahm, M. M.; Evans, D. E.; Schubauer-Berigan, M. K.; Birch, M. E.; Fernback, J. E. *Ann. Occup. Hyg.* **2012**, *56*, 542−556.
(29) Dahm, M. M.; Schubauer-Berigan, M. K.; Evans, D. E.; Birch, M. E.; Fernback, J. E.; Deddens, J. A. *Ann. Occup. Hyg.* **2015**, *59* (6), 705−723.
(30) Lynch, J. A.; Birch, Q. T.; Ridgway, T. H.; Birch, M. E. *Analysis. Ann. Work Expo. Health* **2018**, *62* (5), 604−612.
(31) Murphy, D.; Chow, J.; Leibensperger, E.; Malm, W.; Pitchford, M.; Schichtel, B.; Watson, J.; White, W. *Atmos. Chem. Phys.* **2011**, *11* (10), 4679−4686.
(32) Bahadur, R.; Feng, Y.; Russell, L. M.; Ramanathan, V. *Atmos. Environ.* **2011**, *45* (5), 1162−1167.
(33) Birch, M. E.; Wang, C.; Fernback, J. E.; Feng, H. A.; Birch, Q. T.; Dozier, A. K. Analysis of carbon nanotubes and nanofibers on mixed cellulose ester filters by transmission electron microscopy. *NIOSH Manual of Analytical Methods*, 5th ed.; DHHS (NIOSH) Publication No. 2014-151: Cincinnati, OH, 2017.
(34) Braun, E. I.; Huang, A.; Tusa, C. A.; Yukica, M. A.; Pantano, P. *J. Occup. Environ. Hyg.* **2016**, *13* (12), 915−923.
(35) Dresselhaus, M. S.; Dresselhaus, G.; Saito, R.; Jorio, A. *Phys. Rep.* **2005**, *409* (2), 47−99.
(36) Dresselhaus, M. S.; Jorio, A.; Hofmann, M.; Dresselhaus, G.; Saito, R. *Nano Lett.* **2010**, *10* (3), 751−758.
(37) López-Lorente, A. I.; Simonet, B. M.; Valcárcel, M. *Talanta* **2013**, *105*, 75−79.
(38) Ferrugiari, A.; Tommasini, M.; Zerbi, G. *J. Raman Spectrosc.* **2015**, *46* (12), 1215−1224.
(39) NIOSH. *Approaches to Safe Nanotechnology; Managing the Health and Safety Concerns Associated with Engineered Nanomaterials*; DHHS NIOSH Publication No. 2009-125: Cincinnati, OH, 2009.
(40) Bello, D.; Hart, A. J.; Ahn, K.; Hallock, M.; Yamamoto, N.; Garcia, E. J.; Ellenbecker, M. J.; Wardle, B. L. *Carbon* **2008**, *46* (6), 974−977.
(41) Bello, D.; Wardle, B. L.; Yamamoto, N.; Guzman deVilloria, R.; Garcia, E. J.; Hart, A. J.; Ahn, K.; Ellenbecker, M. J.; Hallock, M. *J. Nanopart. Res.* **2009**, *11* (1), 231−249.
(42) Lee, J. H.; Lee, S.-B.; Bae, G. N.; Jeon, K. S.; Yoon, J. U.; Ji, J. H.; Sung, J. H.; Lee, B. G.; Lee, J. H.; Yang, J. S.; Kim, H. Y.; Kang, C. S.; Yu, I. J. *Inhalation Toxicol.* **2010**, *22* (5), 369−381.
(43) Zheng, L.; Kulkarni, P.; Zavvos, K.; Liang, H.; Birch, M. E.; Dionysiou, D. D. *J. Aerosol Sci.* **2017**, *104*, 66−78.
(44) Diwakar, P. K.; Kulkarni, P. *J. Anal. At. Spectrom.* **2012**, *27* (7), 1101−1109.
(45) Zheng, L.; Kulkarni, P. *Anal. Chem.* **2017**, *89* (12), 6551−6558.
(46) Zheng, L.; Kulkarni, P.; Dionysiou, D. D. *J. Anal. At. Spectrom.* **2018**, *33* (3), 404−412.
(47) Bowie, B. T.; Chase, D. B.; Griffiths, P. R. *Appl. Spectrosc.* **2000**, *54* (6), 200A−207A.
(48) Johansson, J.; Pettersson, S.; Taylor, L. S. *J. Pharm. Biomed. Anal.* **2002**, *30* (4), 1223−1231.
(49) Marigheto, N.; Kemsley, E.; Potter, J.; Belton, P.; Wilson, R. *Spectrochim. Acta, Part A* **1996**, *52* (12), 1571−1579.
(50) Zhang, Y.; Son, H.; Zhang, J.; Kong, J.; Liu, Z. *J. Phys. Chem. C* **2007**, *111* (5), 1988−1992.
(51) Rosasco, G.; Etz, E.; Cassatt, W. *Appl. Spectrosc.* **1975**, *29* (5), 396−404.
(52) Everall, N.; Lumsdon, J.; Christopher, D. *Carbon* **1991**, *29* (2), 133−137.
(53) Kagi, H.; Tsuchida, I.; Wakatsuki, M.; Takahashi, K.; Kamimura, N.; Iuchi, K.; Wada, H. *Geochim. Cosmochim. Acta* **1994**, *58* (16), 3527−3530.
(54) John, W. S. Sampling Respirable and Fine Aerosol. In *Particle Size-Selective Sampling for Particulate Air Contaminants*; Vincent, J. H., Ed.; American Conference of Governmental Industrial Hygienists (ACGIH): Cincinnati, OH, 1999.
(55) Mahajan, A.; Kingon, A.; Kukovecz, A.; Konya, Z.; Vilarinho, P. M. *Mater. Lett.* **2013**, *90*, 165−168.
(56) Cataldo, F. *Fullerenes, Nanotubes, Carbon Nanostruct.* **2002**, *10* (4), 293−311.
(57) Datsyuk, V.; Kalyva, M.; Papagelis, K.; Parthenios, J.; Tasis, D.; Siokou, A.; Kallitsis, I.; Galiotis, C. *Carbon* **2008**, *46* (6), 833−840.
(58) NIOSH. *Components for Evaluation of Direct-Reading Monitors for Gases and Vapors*; DHHS, U.S.: Washington, DC, 2012.
(59) Esswein, E. J.; Alexander-Scott, M.; Snawder, J.; Breitenstein, M. *J. Occup. Environ. Hyg.* **2018**, *15* (1), 63−70.
(60) Sheesley, R. J.; Schauer, J. J.; Smith, T. J.; Garshick, E.; Laden, F.; Marr, L. C.; Molina, L. T. *J. Environ. Monit.* **2008**, *10* (3), 305−314.
(61) Bott, R. C.; Kirk, K. M.; Logan, M. B.; Reid, D. A. *Environ. Sci.: Processes Impacts* **2017**, *19* (10), 1320−1326.
(62) Dippel, B.; Heintzenberg, J. *J. Aerosol Sci.* **1999**, *30*, S907−S908.
(63) Gruber, T.; Zerda, T. W.; Gerspacher, M. *Carbon* **1994**, *32* (7), 1377−1382.
(64) Jawhari, T.; Roid, A.; Casado, J. *Carbon* **1995**, *33* (11), 1561−1565.
(65) Nic, M.; Hovorka, L.; Jirat, J.; Kosata, B.; Znamenacek, J. *IUPAC Compendium of Chemical Terminology-The Gold Book*; International Union of Pure and Applied Chemistry: 2005.
(66) Bae, M.-S.; Schauer, J. J.; DeMinter, J. T.; Turner; Smith, D. *Atmos. Environ.* **2004**, *38* (18), 2885−2893.
(67) Turpin, B. J.; Cary, R. A.; Huntzicker, J. J. *Aerosol Sci. Technol.* **1990**, *12* (1), 161−171.
(68) Volotskova, O.; Shashurin, A.; Keidar, M.; Raitses, Y.; Demidov, V.; Adams, S. *Nanotechnology* **2010**, *21* (9), 095705.
(69) Mertes, S.; Dippel, B.; Schwarzenböck, A. *J. Aerosol Sci.* **2004**, *35* (3), 347−361.
(70) Sze, S.-K.; Siddique, N.; Sloan, J.; Escribano, R. *Atmos. Environ.* **2001**, *35* (3), 561−568.
(71) Cançado, L.; Takai, K.; Enoki, T.; Endo, M.; Kim, Y.; Mizusaki, H.; Jorio, A.; Coelho, L.; Magalhaes-Paniago, R.; Pimenta, M. *Appl. Phys. Lett.* **2006**, *88* (16), 163106.
(72) Casiraghi, C.; Hartschuh, A.; Qian, H.; Piscanec, S.; Georgi, C.; Fasoli, A.; Novoselov, K.; Basko, D.; Ferrari, A. *Nano Lett.* **2009**, *9* (4), 1433−1441.
(73) Jiang, J.; Pachter, R.; Mehmood, F.; Islam, A. E.; Maruyama, B.; Boeckl, J. J. *Carbon* **2015**, *90*, 53−62.
(74) Sato-Berrú, R.; Basiuk, E.; Saniger, J. *J. Raman Spectrosc.* **2006**, *37* (11), 1302−1306.
(75) Saffaripour, M.; Tay, L.-L.; Thomson, K. A.; Smallwood, G. J.; Brem, B. T.; Durdina, L.; Johnson, M. *Aerosol Sci. Technol.* **2017**, *51* (4), 518−531.
(76) Suhartono, L.; Cornilsen, B. C.; Johnson, J. H.; Carlson, D. H. *Appl. Occup. Environ. Hyg.* **1996**, *11* (7), 790−798.
(77) Sadezky, A.; Muckenhuber, H.; Grothe, H.; Niessner, R.; Pöschl, U. *Carbon* **2005**, *43* (8), 1731−1742.
(78) Bokobza, L.; Bruneel, J.-L.; Couzi, M. *Chem. Phys. Lett.* **2013**, *590*, 153−159.
(79) Catelani, T.; Pratesi, G.; Zoppi, M. *Aerosol Sci. Technol.* **2014**, *48* (1), 13−21.
(80) Barnes, R.; Dhanoa, M. S.; Lister, S. J. *Appl. Spectrosc.* **1989**, *43* (5), 772−777.
(81) Chernyak, S. A.; Ivanov, A. S.; Maslakov, K. I.; Egorov, A. V.; Shen, Z.; Savilov, S. S.; Lunin, V. V. *Phys. Chem. Chem. Phys.* **2017**, *19* (3), 2276−2285.
(82) Osswald, S.; Flahaut, E.; Gogotsi, Y. *Chem. Mater.* **2006**, *18* (6), 1525−1533.
(83) Aggarwal, R.; Di Cecca, S.; Farrar, L.; Jeys, T. *J. Raman Spectrosc.* **2014**, *45* (8), 677−679.
(84) Sinanis, S.; Aleksandrova, M.; Schaber, K. *Aerosol Sci. Technol.* **2011**, *45* (6), 751−757.
(85) Stowers, M.; Friedlander, S. *Aerosol Sci. Technol.* **2002**, *36* (1), 48−61.
(86) Doughty, D. C.; Hill, S. C. *J. Quant. Spectrosc. Radiat. Transfer* **2017**, *188*, 103−117.
(87) Grafen, M.; Nalpantidis, K.; Platte, F.; Monz, C.; Ostendorf, A. *Aerosol Sci. Technol.* **2015**, *49* (10), 997−1008.

DOI: 10.1021/acs.analchem.9b02178
Anal. Chem. 2019, 91, 12713−12723

(88) Grafen, M.; Schweiger, G.; Esen, C.; Ostendorf, A. *J. Aerosol Sci.* **2018**, *117*, 34−43.
(89) Bounos, G.; Andrikopoulos, K. S.; Karachalios, T. K.; Voyiatzis, G. A. *Carbon* **2014**, *76*, 301−309.
(90) Anoshkin, I. V.; Nefedova, I. I.; Lioubtchenko, D. V.; Nefedov, I. S.; Räisänen, A. V. *Carbon* **2017**, *116*, 547−552.
(91) Bokobza, L.; Bruneel, J.-L.; Couzi, M. *Carbon* **2015**, *1* (1), 77−94.
(92) Ko, H.; Pikus, Y.; Jiang, C.; Jauss, A.; Hollricher, O.; Tsukruk, V. V. *Appl. Phys. Lett.* **2004**, *85* (13), 2598−2600.

DOI: 10.1021/acs.analchem.9b02178
Anal. Chem. 2019, 91, 12713−12723